

# Morphing Origami Block for Lightweight Reconfigurable System

Sa-Reum Kim, *Student Member, IEEE*, Dae-Young Lee , Sang-Joon Ahn , *Student Member, IEEE*, Je-Sung Koh , *Member, IEEE*, and Kyu-Jin Cho , *Member, IEEE*

## I. INTRODUCTION

**Abstract**—Origami provides a unique tool for the design of robotic frames owing to its simple shaping principle by “folding.” However, achieving the fast and reversible activeness of a highly reconfigurable structure remains challenging owing to the limitations of accessible actuators. In particular, it is difficult to find an actuator that can realize a simultaneously large, rapid, reversible, and stable movement while leading to a favorable form factor for the origami. To overcome this, in this article, we propose a 3-D shape-shifting system consisting of a morphing origami block that complements the stability problem of shape memory alloy wire actuators by tuning its structural characteristics. This cooperative scheme improves the reversibility and stability of the shape-shifting system, which enables the rapid transformation with high degrees of freedom unlike in existing programmable origami. As a stand-alone unit of transformation, morphing block equipped with deployable mechanism and actuators weighs 6 g and has a volume change factor of ten. Furthermore, the transformation time in both directions is less than 5 s, and the block can carry more than 120 g of payload in the deployed state. The proposed system composed of multiple origami blocks can reconfigure itself into diverse 3-D target shapes.

**Index Terms**—Compliant mechanism, mechanism design, modular robots, robotic origami.

Manuscript received January 27, 2020; revised June 18, 2020; accepted September 3, 2020. Date of publication November 11, 2020; date of current version April 2, 2021. This work was supported in part by the Korean Government through the National Research Foundation of Korea (NRF) under Grant NRF-2016R1A5A1938472 and Grant NRF-2020M1A3B8084924, in part by the New Faculty Research Fund of Ajou University, and in part by the Ajou University Research Fund. This article was recommended for publication by Associate Editor J. Paik and Editor M. Yim upon evaluation of the reviewers’ comments. (Sa-Reum Kim and Dae-Young Lee contributed equally to this work.) (Corresponding author: Kyu-Jin Cho).

Sa-Reum Kim is with the Department of Mechanical Engineering, University of California, Berkeley, CA 94720 USA, and also with the Soft Robotics Research Center, Department of Mechanical Engineering, Seoul National University, Seoul 08826, South Korea (e-mail: sareum@berkeley.edu).

Dae-Young Lee is with the School of Engineering and Applied Sciences, Harvard University, Cambridge, MA 01451 USA, and also with the Soft Robotics Research Center, Department of Mechanical Engineering, Seoul National University, Seoul 08826, South Korea (e-mail: dylee@seas.harvard.edu).

Sang-Joon Ahn and Kyu-Jin Cho are with the Soft Robotics Research Center, Department of Mechanical and Aerospace Engineering and the Institute of Advanced Machines and Design, Seoul National University, Seoul 08826, South Korea (e-mail: ghiip203@gmail.com; kjcho@snu.ac.kr).

Je-Sung Koh is with the Department of Mechanical Engineering, Ajou University, Suwon 16499, South Korea (e-mail: jskoh@ajou.ac.kr).

This article has supplementary downloadable multimedia material available at <http://ieeexplore.ieee.org> provided by the authors. This includes a video which shows the performances and characteristics of the reconfigurable system and its elements mentioned in the manuscript. The material is 14.9MB in size.

Color versions of one or more of the figures in this article are available online at <https://ieeexplore.ieee.org>.

Digital Object Identifier 10.1109/TRO.2020.3031248

ORIGAMI has been proved to be a unique tool for developing transformable structures in natural [1]–[4] and artificial systems [5], [6]. The simple shaping principle of origamis, i.e., the transformation between a planar (2-D) packed shape and a desired 3-D shape by folding and unfolding along predefined crease lines, has been adopted in the robotics field for various purposes. The lightweight skeletal structure enabled by origamis is extremely advantageous to realize robotic applications in challenging environments, such as dynamic gaits in unstructured terrains [7], wing transmission [8], jumping on water [9], foldable arms for an unmanned aerial vehicles (UAVs) [10], deployable robots with dual morphing [11], and multimodal locomotion [12], [13]. Another advantage of origami structures is the dramatic and versatile shape-changing capability without the need for a complex assembly process. This aspect has been exploited for various applications, such as a deployable wheel [14], self-deployable stents [15], and foldable UAV [16]. In addition, researchers have focused on the benefits of the simplicity of origami-style fabrication as a potential means to expand the accessibility of robotics to the public [17] and to allow the development of self-assembly robots [18]–[20].

To fully exploit the advantages of the transformability of origami structures, researchers attempted to develop shape-programmable origamis. The theory of origami proves that an infinite number of arbitrary 3-D shapes can be generated from a 2-D template [21], [22], and various methods have been proposed for implementing programmability, such as universal self-folding sheets [23], [24], mechanical metamaterials [25]–[29], Snapology [30], tessellation [31], lattice kirigamis [32], and string origamis [33].

Although many methods to achieve programmable origami have been reported, it has been challenging to realize active programmable origami that can exhibit large, rapid, reversible, and stable movement in real-world applications. Programmable matter by folding [23] with multiple degrees of freedom (DOF) actuation was achieved by using a distributed self-folding joint made of a shape memory alloy (SMA) actuator. A robotic origami module was built using conventional electric motors to realize a small-distance and simple folding motion [34]. A metamaterial machine was developed using fast and reversible pneumatic actuation on hinges to provide multi-DOF transformation into various configurations [25]. Fast and reversible folding was achieved using ferromagnetic domains [35] or fluidic channels [36]. The critical factor determining the performance of

the active programmable origami is the limitation of the folding actuator.

In the previous study, we proposed a fast and reversible self-folding block array consisting of a torsional SMA wire (TSW) actuator [37] in a conference form [38]. In these studies, we presented the concept of a stand-alone unit of transformation by using an overconstrained origami pattern to achieve bistability. The discretization of the entire morphing architecture into numerous identical morphing blocks with simple binary transformation allowed high-DOF shaping control without suffering from highly nonlinear characteristics of actuation; the torque depends on the location and configuration of the actuator, which was a major obstacle to achieve the target shape.

However, the presented origami blocks can only be deployed in a 2-D plane and cannot be expanded into 3-D space direction due to the low structural stability after transformation. Even though the high energy density of a TSW actuator provides a high driving force, the blocking force of the actuator is insufficient to maintain the structure without an accompanying motion and additional energy consumption.

In this study, we demonstrate a programmable origami architecture with 3-D shape-changing capability and its enabling design methodology to create desired actuation characteristics without the need for additional actuators or components. We present a method to systematically design active origamis based on the cooperative scheme between the physical property of the origami structures (structural bistability) and a low-profile origami-compatible actuator (TSW actuator) to balance the stability and transformability of the origami mechanism. The key strategy is to exploit the multi-DOF behavior of a flexure under the overconstrained kinematics by understanding the behavior of two origami components—the facet and flexure. Unlike most of the existing origami models, which consider thin flexures as joints with a single DOF and facets as rigid links without deformation, we modeled both deformations and determined the contribution of each component to the global folding deployment of the origami composite. As a result, we can tune the bistability by changing the lengths of the flexure so that the block can generate an additional DOF with a unique torque profile. Furthermore, we selected an efficient actuator location by considering the nonlinear behavior of the structure to ensure the minimization of the required torque for the target transformation.

The proposed system demonstrated a fast and reversible morphing capability with mechanical stabilization features. Each block (see Fig. 1) is a self-contained and lightweight (6 g) unit that can rapidly change its shape (within 5 s) with a high deformation ratio (volume change factor of ten). Furthermore, each block can support at least 20 and five times its own weight in the static and transition states, respectively. The modularity concept is proven through the development of a 3-D reconfigurable system with 27 morphing blocks arranged in a  $3 \times 3 \times 3$  lattice. The presented system provides a shape-programmable architecture owing to the use of the collective binary shape switching of the blocks into various 3-D target configurations.

## II. STRUCTURE DESIGN

The morphing block structure design is inspired by the Kresling origami pattern [39], which is a flat-foldable, deployable

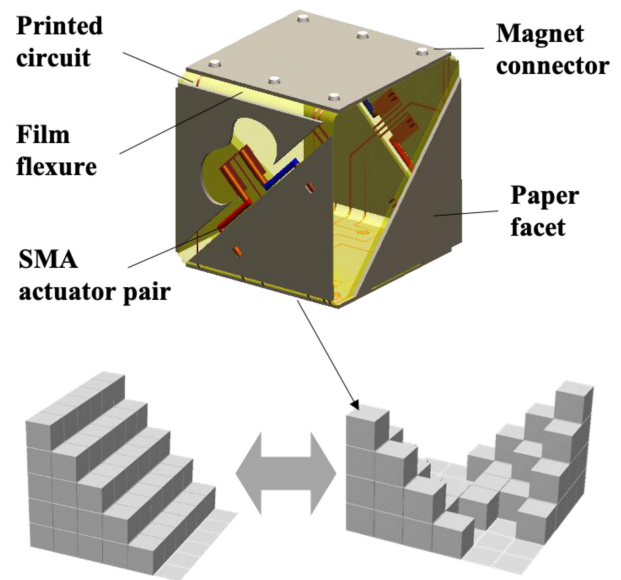


Fig. 1. Three-dimensional programmable origami consists of a multitude of morphing origami blocks. Blocks are identical, self-contained units that contain folding mechanism for deployment, two pairs of self-folding actuators on the side facets, printed circuits on the flexures, and magnet electrodes.

column. This pattern has been used as a kinematic bone structure for various transforming applications, such as deployable columns [40] and mechanical metamaterials [41]. The triangular facets of the Kresling pattern enable a column to be expandable and collapsible through the simultaneous vertical and rotational motions of the top surface, which leads to a dramatic volume change. Such a pattern exhibits bistability owing to its geometry, which can help realize coupled torsional and elongated motion in an orthogonal manner. This bistability makes a target configuration more stable than the other configurations that can appear during continuous transformation and helps generate rapid snap-through motion. Although the original pattern has a connected column structure, each layer of the column can be decoupled from the others, as the pattern can be transformed in both localized and global manners. In addition, because the base shape and footprint area of each module remain constant during the transformation, the transforming unit is stackable.

Considering that the Kresling pattern is compatible with any polygonal base shape, we attempted to use the simplest pattern that can generate a unit volumetric change. The minimum requirements of the polygonal base were as follows: 1) the tessellated pattern can fill the plane without gaps and 2) the height of the polyprism is equal to or larger than the side length of a polygon (in order to allow a large volumetric change). The simplest case of planar tessellation is an equilateral triangle. To determine the maximum height of the polyprism for each polygon, we plotted the vertexes on the circumscribed circle of the polygon. The top and bottom facets were assumed to move parallel to each other during the deployment. As shown in Fig. 2(a), which shows the top view of the circumscribed circle, the height is maximized as  $\overline{AC}$  passes through the center of the circle (critical case) with only half of its side length. The second simplest candidate that satisfies planar tessellation is a square. As shown in Fig. 2(b), the maximum height is equal to the side

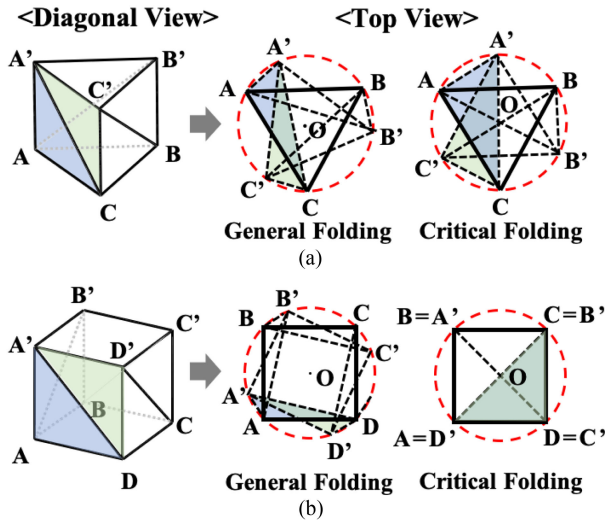


Fig. 2. Folding pattern generation for the origami block. (a) Equilateral triangle case and its top view in the general and critical folding cases. (b) Square case and its top view in the general and critical folding cases.

length of the square. Therefore, we selected the square polygon case of a Kresling pattern for the morphing block.

### III. TUNING OF THE PHYSICAL CHARACTERISTICS

The key physical characteristics of the morphing block are stability against mechanical disturbances and the presence of an energy barrier to prevent spontaneous state transitions. To ensure these characteristics, we used origami patterns with bistability [42]–[44], which have inherent stability in certain configurations. If the crease lines of the origami pattern are assumed as ideal revolute joints according to the traditional origami models [45], [46], the kinematics of the morphing block derived from the Kresling pattern can be defined only in two states, namely, a fully folded sheet state and a fully deployed cubic state. Moreover, as the block moves from one state to the other, it undergoes undefined kinematic configurations due to the extra mobility afforded by the elastic deformation of the materials [47]. The origami pattern of the block consists of two types of elements made of different materials—the rigid facets and the flexible joints (flexures) connecting the facets. The response of each part with different stiffnesses leads to a unique physical characteristic, which is useful for the tuning of the physical characteristics. In this study, two geometrical factors were introduced to tune the physical characteristics—the modification of a connected pattern and the variation of the flexure lengths. The disconnection of the faces can change the skeletal structure of the block, which can lead to a dramatic variation in the energy barrier according to the deformation mode. In contrast, the use of the flexure length allows the fine-tuning of the energy barrier.

#### A. Kinetic Chain Modeling (Facet Characteristic Model)

Fig. 3 shows the possible facet configurations. The top and bottom plates are connected through multiple kinetic chains (represented as red lines in Fig. 3). These kinetic chains in a

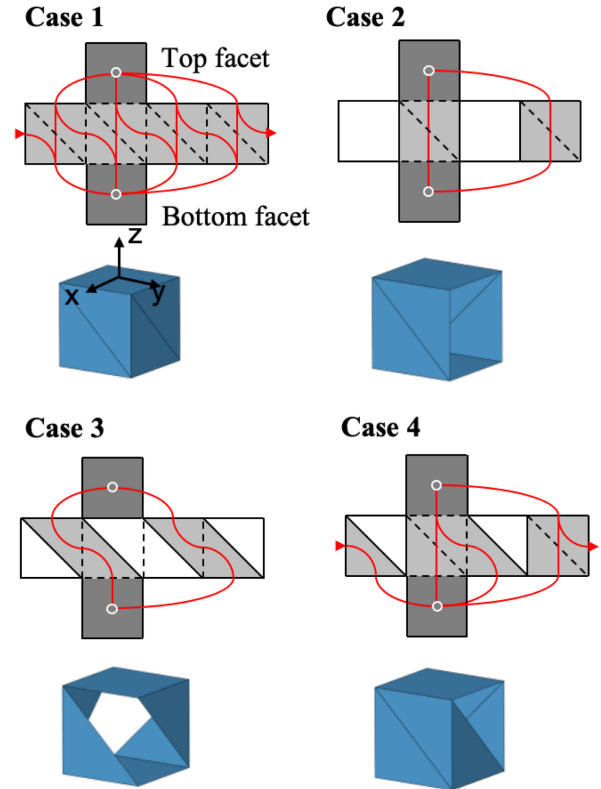


Fig. 3. Cases of facet separations. The number and shape of the kinetic chains determine the possible deformation modes of the block.

closed-loop reduce the freedom of movement, thereby helping in the realization of the desired shape transformation. However, the quantitative examination of the physical effect of the chains is challenging owing to their complex 3-D behavior and high geometrical nonlinearity.

In this study, we analyzed the effects of the chains rather than performing an exhaustive analysis of the mechanics of the compliant material. We built a simplified truss model assuming that the deformation of the facet is negligible compared to the facet dimension (see Fig. 4). Each facet was modeled as a combination of trusses (i.e., virtual linear springs), and the deformation of each facet was represented by the compression of the springs, which were not allowed to undergo stretching. The deformation of the facet was quantified from the internal energy of the structure  $U_F$ , which is proportional to the sum of the squared displacements of the facet springs; however, the following condition had to be satisfied—the dislocation of a connecting vertex should remain in the flexure length range. We assumed that the structure was always deformed in the direction leading to the minimum  $U_F$ . Based on these assumptions, the problem of obtaining the configuration of the structure can be expressed as the following optimization problem:

$$\begin{aligned} & \text{minimize } U_F \\ & = k_F \sum_{mij} \frac{(\|{}^m\mathbf{V}_i - {}^m\mathbf{V}_j\| - l_{Fmij})^2}{l_{Fmij}} \end{aligned}$$

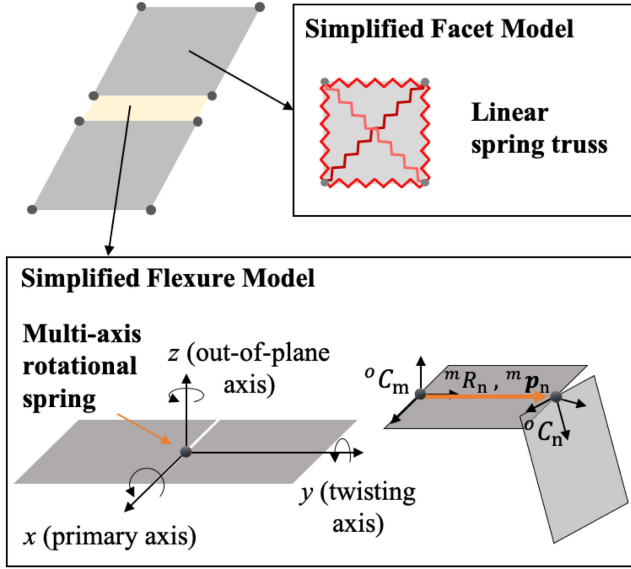


Fig. 4. Simplified model for the facet and flexure deformation. The facet is treated as a truss structure with elasticity (only compression), and the flexure is treated as a multi-axis rotational spring whose stiffness changes depending on the direction of the bend.

$$\text{subject to } \| {}^m \mathbf{V}_i - {}^n \mathbf{V}_j \| - l_f < 0$$

$$\text{for all the interfacet vertex pairs } (m, n, i, j) \quad (1)$$

where  $k_F$  is the effective stiffness of the facet model,  ${}^m \mathbf{V}_i$  is the position vector of the  $i$ th vertex of the  $m$ th facet,  $l_{F_{mij}}$  is the undeformed length of the truss connecting the  $i$ th and  $j$ th vertices of the  $m$ th facet, and  $l_f$  is the length of the flexure. Because the work applied to the structure had a direct impact on the internal energy, the gradient of  $U_F$  was assumed to represent the responsive force. A vertex configuration of the block was created by finding a configuration corresponding to the minimum  $U_F$  by using the sequential quadratic programming algorithm provided by MATLAB, MathWorks.

Fig. 5(a) shows the response of the structure to a disturbance, as calculated using the model, and Fig. 5(b) shows photographs of the blocks. For each case, the resistive forces were investigated by applying a relative displacement of 20% to the top facet in the  $x$ -,  $y$ -, and  $z$ -directions. Case 1, which corresponds to the original pattern without a disconnection, contains the full set of kinetic chains, which provides a large disturbance resistance in all directions. However, the four layers of facets between the top and bottom facets thicken the structure when fully folded. Case 2 involves a simple circular loop of the kinetic chains with four side facets. Although removing the side facets solves the interference and thickness problems, this configuration causes undesired excessive movement, resulting in a low resistive force against the disturbances in the  $x$ -direction. Case 3 is another case in which the side facets are removed. Although the twisted kinetic chain leads to a kinematic overconstraint, the structure lacks mechanical stability as it can undergo large displacements even with a small facet deformation. Case 4, the selected pattern, includes half of the original kinetic chains, with three side facets

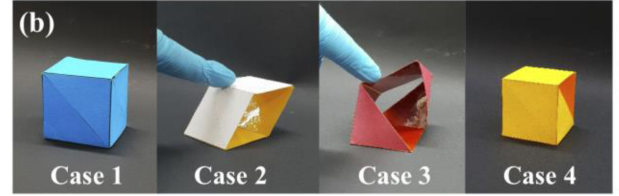
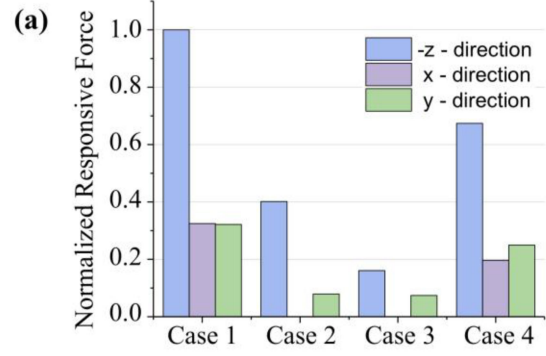


Fig. 5. (a) Responsive force against the displacements in the  $x$ ,  $y$ , and  $z$  directions. Cases 2 and 3 do not involve a resistance against the deformation in the  $x$ -direction. (b) Photographs of the blocks showing the response of each pattern to the external force. The presence of an insufficient resistance leads to undesired deformation modes.

in each chain. The superposition of the kinetic chains in different shapes leads to high resistance in all directions.

### B. Flexure Characteristic Modeling

A flexure connecting a facet pair serves as a joint of an origami structure, and it is generally expected to have a single DOF along a predefined direction. However, in practical scenarios, a flexure typically has additional DOFs, and thus, is important for the transformation between stable states in the proposed structure. Nevertheless, an exhaustive analysis of the characteristic of flexure is challenging owing to its complex behavior. To simplify this problem, we assumed that the flexure always has a developable surface and solely considered a relative rotation between the facets by neglecting the relative translation allowed by the flexure. We assumed the flexure to be a multi-axis rotational spring with a rotational stiffness, which is a function of the rotation vector. To derive the correlation function between the rotation vector and rotational stiffness, we focused on the effect of the direction of the rotation. In general, the rotation direction vector should be aligned along the primary axis. However, because the overconstrained condition of the structure induces out-of-plane and twisting axis components, we assumed that this misalignment affected the size of the bending area, resulting in a dramatic change in the rotational stiffness of the flexure joint.

We denote the set of basis vectors of the coordinate system of the  $m$ th facet with respect to the origin coordinate as  ${}^o C_m \in \text{SO}(3)$  and the rotation matrix from the basis of the  $m$ th facet to the  $n$ th facet as  ${}^m \mathcal{R}_n \in \text{SO}(3)$ . Then, the rotation matrix can be transformed into a unique rotation vector as follows:

$${}^m \mathcal{R}_n \mapsto {}^m \phi_n = ({}^m \phi_{nx}, {}^m \phi_{ny}, {}^m \phi_{nz}) \quad (2)$$

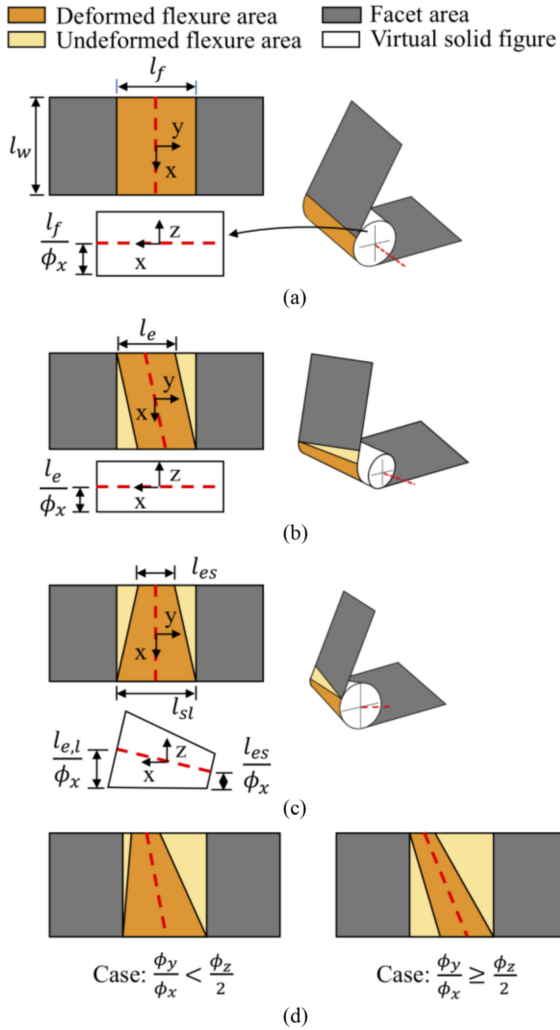


Fig. 6. Change in the bending area as a function of the rotation direction. (a) Bending in predefined direction. (b) Bending area reduction induced by the  $\phi_y$  component. (c) Bending area reduction induced by the  $\phi_z$  component. (d) Diagram of the effective lengths of the long ( $l_{el}$ ) and short sides ( $l_{es}$ ).

where, in this study, we consider vector  ${}^m\mathcal{R}_n$  as an indicator of the flexure deformation (see Fig. 4). The accumulated strain energy of the flexure was assumed as a function of the rotation vector as

$$U_f = \sum_{mn}^{k_f} \|{}^m\phi_n\|^2, \quad k_f = g({}^m\phi_n). \quad (3)$$

It is worth noting that the rotational stiffness  $k_f$  is a function of the rotation vector  ${}^m\phi_n$ .

The correlation function was derived under the assumption that the flexure is inextensible, and thus, the deformed surface remains in the developable surface; in other words, the deformed surface can be flattened onto a plane without an axial membrane strain. Under this assumption, we introduced the virtual solid figure shown in Fig. 6 to describe the behavior of the flexure. Owing to the characteristic of the developable surface, the flexure can be assumed to behave as if it wraps the virtual cylinder;

then, the central axis of the cylinder becomes a rotation axis of the flexure.

If the rotation vector has a twisting axis component  $\phi_y$ , the configuration of the cylinder moves, as shown in Fig. 6(b), and reduces the deformed area of the flexure. The deformation area is determined from the effective length  $l_e$ , which can be calculated as

$$l_e = l_f - l_w \frac{\phi_y}{\phi_x} \quad (4)$$

where  $l_f$  and  $l_w$  denote the length and width of the flexure, respectively. The change in the rotation axis according to the out-of-plane component  $\phi_z$  can be described by transforming the cylinder into a truncated cone, as shown in Fig. 6(c). The effective lengths of the long side  $l_{el}$  and short side  $l_{es}$  can be defined as

$$l_{el} = l_f \quad (5)$$

$$\frac{l_{el} - l_{es}}{l_w \phi_x} = \frac{\phi_z}{\phi_x}, \quad l_{es} = l_f - l_w \phi_z. \quad (6)$$

By combining these factors, as shown in Fig. 6(d), the resultant effective length can be calculated as

$$l_{el} = \begin{cases} l_f, & \text{if } \frac{\phi_y}{\phi_x} < \frac{\phi_z}{2} \\ l_f - l_w \left( \frac{\phi_y}{\phi_x} - \frac{\phi_z}{2} \right), & \text{otherwise} \end{cases} \quad (7)$$

$$l_{es} = \begin{cases} l_f - l_w \phi_z, & \text{if } \frac{\phi_y}{\phi_x} < \frac{\phi_z}{2} \\ l_f - l_w \left( \frac{\phi_y}{\phi_x} + \frac{\phi_z}{2} \right), & \text{otherwise} \end{cases}. \quad (8)$$

If we assume that the material has linear material property and pure bending, the strain energy of the flexure can be expressed as

$$U_{fmn} = \frac{Dl_w}{2} \int_{l_e} \left( \frac{\|{}^m\phi_n\|}{l_e} \right)^2 ds = \frac{Dl_w}{2} \cdot \frac{1}{l_e} \|{}^m\phi_n\|^2, \quad (9)$$

$$k_f = \frac{Dl_w}{2} \cdot \frac{1}{l_e}, \quad D = \frac{Eh^3}{12(1-\nu^2)}$$

where  $E$  is the Young's modulus,  $h$  is the flexure thickness,  $D$  is the flexural rigidity, and  $\nu$  is the Poisson's ratio. According to (9), the rotational stiffness is inversely proportional to the effective flexure length. By assuming the linear variation from  $l_{es}$  to  $l_{el}$ , the average value of the rotational stiffness can be calculated as

$$k_f = \frac{Dl_w}{2} \cdot \frac{1}{l_{el} - l_{es}} \int_{l_{es}}^{l_{el}} \frac{1}{s} ds = \frac{Dl_w}{2} \cdot \frac{\ln l_{el} - \ln l_{es}}{l_{el} - l_{es}}. \quad (10)$$

From (4), (7), (8), and (10), we have

$$k_f = \begin{cases} \frac{D}{2} \cdot \frac{1}{\phi_z} \ln \frac{1}{1 - \frac{l_w}{l_f} \phi_z}, & \text{if } \frac{\phi_y}{\phi_x} < \frac{\phi_z}{2} \\ \frac{D}{2} \cdot \frac{1}{\phi_z} \ln \frac{1 - \frac{l_w}{l_f} \left( \frac{\phi_y}{\phi_x} - \frac{\phi_z}{2} \right)}{1 - \frac{l_w}{l_f} \left( \frac{\phi_y}{\phi_x} + \frac{\phi_z}{2} \right)}, & \text{otherwise} \end{cases}. \quad (11)$$

As  $\phi_y$  or  $\phi_z$  increases,  $k_f$  approaches infinity, which is physically impossible; this is probably caused by the nonlinearity of the material and buckling deformation. To prevent the singularity in the model while maintaining the general tendency,

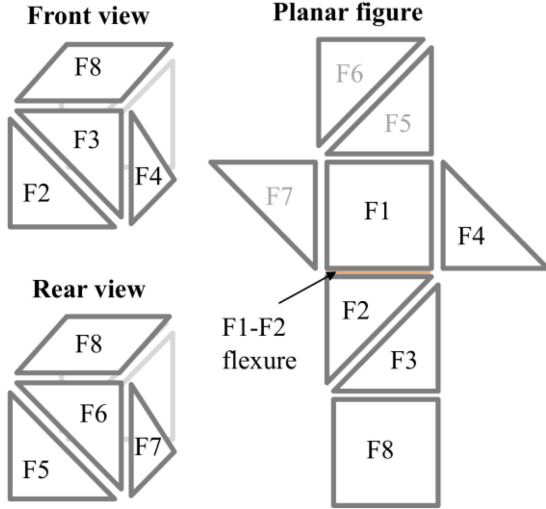


Fig. 7. Facet and flexure map for the origami block.

we approximated (11) by limiting the order of the equation  $\lambda$  in the series expansion form as follows:

$$k_f = \begin{cases} \frac{D}{2} \cdot \sum_{n=1}^{\lambda} \frac{1}{n} \left( \frac{l_w}{l_f} \right)^n \phi_z^{n-1}, & \text{if } \frac{\phi_y}{\phi_x} < \frac{\phi_z}{2} \\ \frac{D}{2} \sum_{n=1}^{\lambda} \frac{1}{n} \left( \frac{l_w}{l_f} \right)^n \left[ \frac{\left( \frac{\phi_y}{\phi_x} + \frac{\phi_z}{2} \right)^n - \left( \frac{\phi_y}{\phi_x} - \frac{\phi_z}{2} \right)^n}{\phi_z} \right], & \text{otherwise} \end{cases} \quad (12)$$

The constraint equation is derived from the kinematics of the facet kinetic chain. Considering the rotation matrix  ${}^m\mathcal{R}_n$  and the position vector of the rotation point  ${}^m\mathbf{p}_n$ , the transformation matrix can be defined as follows:

$${}^m T_n = \begin{bmatrix} {}^m\mathcal{R}_n & {}^m\mathbf{p}_n \\ 0 & 1 \end{bmatrix} \in \text{SE}(3). \quad (13)$$

The facet map of the structure is shown in Fig. 7. Considering the geometrical constraints of the top facet (facet 8), we obtain

$$C = {}^o T_1 {}^1 T_2 {}^2 T_3 {}^3 T_8. \quad (14)$$

Furthermore, from the chain loop of the facet 1-2-3-4, we obtain

$$I = {}^o T_1 {}^1 T_2 {}^2 T_3 {}^3 T_4 {}^4 T_1. \quad (15)$$

Using (3), (12), (14), and (15), the realization of the configuration of the structure considering the flexure deformation can be defined in the following optimization problem form:

$$\begin{aligned} & \underset{\phi \in \mathbb{R}^{12}}{\text{minimize}} \quad U_f = \sum_{mn}^{k_f} \| {}^m \phi_n \|^2 \\ & \text{subject to} \quad C - {}^o T_1 {}^1 T_2 {}^2 T_3 {}^3 T_8 = 0 \\ & \quad \quad \quad I - {}^o T_1 {}^1 T_2 {}^2 T_3 {}^3 T_4 {}^4 T_1 = 0. \end{aligned} \quad (16)$$

In this study, the optimization problem was solved using the MATLAB, MathWorks optimization solver through the sequential quadratic programming method.

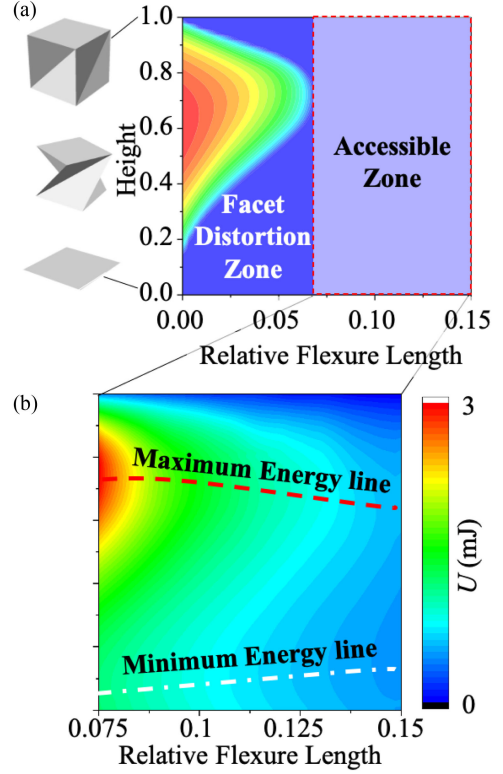


Fig. 8. Simulation results of estimating deformation energy. (a) Plot of deformation energy  $U_F$  resulting from the facet deformation with the change in the relative flexure length. If the relative flexure length is at least 7.5%, the facet deformation can be avoided. (b) Plot of the deformation energy  $U_F$  resulting from the flexure deformation with the change in the relative flexure length.

Fig. 8(a) presents the simulation result obtained with (1) as the flexure length relative to the varying side length of the facet. As the structure compresses, flexure deformation occurs; however, when the limit is reached, the facets begin to deform as well. Because the facets have a higher stiffness than the flexure, they require a higher force to deform, which can also lead to the occurrence of structural failure and delamination owing to the accumulation of damage. Thus, we concluded that to realize the design of the physical properties, it is desirable to avoid the facet deformation by using the flexure deformation to pass through the undefined kinematic configurations. The model predicts that a relative flexure length of approximately 7.5% is the minimum threshold to avoid the facet deformation. For a relative flexure length of 7.5% or more, the flexure deformation model (16) was used to simulate the behavior of the structure [see Fig. 8(b)]. The model shows that it is possible to induce bistability using only the flexure design (without facet deformation). However, as the relative flexure length increases, the maximum  $U_f$  decreases drastically, which reduces the stability in the target configuration. Furthermore, the minimum  $U_f$  increases, which leads to incomplete folding in the folded state. Thus, a relative flexure ratio closer to 7.5% leads to better performance.

### C. Experiment

We conducted two experiments to evaluate the change of the maximum deformation energy and the performance degradation

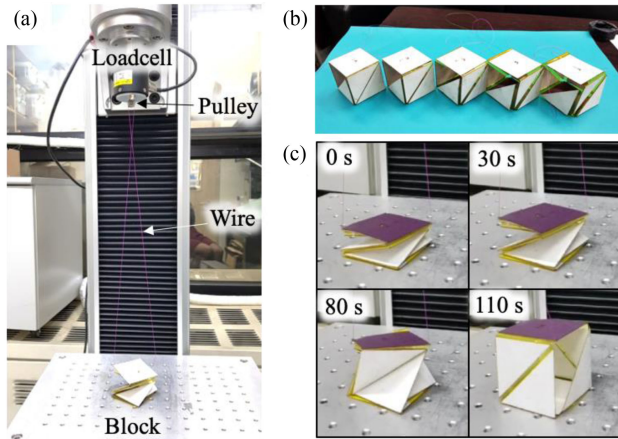


Fig. 9. Flexure experiment setup. (a) Experimental setup with tensile tester. (b) Origami block specimens with various flexure lengths. (c) Screenshot of passive deformation by tensile tester.

TABLE I  
PARAMETERS OF THE SIMULATION OF THE FLEXURE EFFECT

Symbol	Value
$E$ (Young's modulus)	2.5 GPa [48]
$\nu$ (Poisson ratio)	0.34 [48]
$h$ (Material thickness)	12.5 $\mu\text{m}$
$\lambda$ (Estimation order)	4 (Experimental fitting)

owing to repeated actuation. Five specimens were prepared with fixed side length (50 mm) and varied relative flexure length (5%, 7.5%, 10%, 12.5%, and 15%). In the experiment, the force required during the whole deployment is used to measure the deformation energy.

The experimental setup for measuring the deformation energy is shown in Fig. 9. The block was artificially deployed by a wire attached to the diagonal vertex at the top facet to allow the pulling along with a torsional displacement while deploying the unit. To validate the structural characteristics, the specimens were made as a sandwiched origami composite with a thin flexure (polyimide film, thickness of 12.5  $\mu\text{m}$ ) and facet (paper, thickness of 100  $\mu\text{m}$ ) without actuators. The origami block was pulled in the vertical direction by using a tensile tester (RB302; Unitech) at a constant speed of 20 mm/min to transform the block from a folded sheet to an unfolded cube. The pulling pulley was connected to the load cell, which measured the vertical force at a collection rate of 3 Hz (see Fig. 9).

Fig. 10(a) shows the maximum deformation energy measured during the experiments. The plot shows a dramatic energy reduction at a relative flexure length of 7.5%, as predicted in the simulation derived in Section III. The simulation results of (16) were illustrated with the experimental results in Fig. 10(a). The parameters of the simulation obtained from the reference and actual geometries are presented in Table I; the estimation order was determined from the experimental results.

Fig. 10(b) shows the degradation of the maximum deformation energy with repeated deployment. It can be seen that the performance is drastically reduced at the relative flexure lengths of 5%, while the performance is maintained for all the models

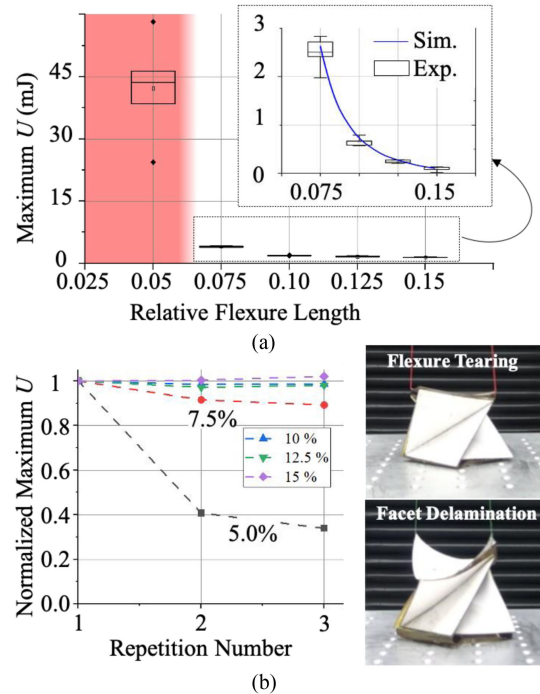


Fig. 10. (a) Experimental and simulation results of the energy required for transformation; the red zone represents the facet distortion zone, which requires large energy. (b) Degradation of the structure during repeated actuation.

with a relative flexure length of at least 7.5%. The presence of the small flexures leads to large deformations in the facet and consequent structural failure.

#### IV. ACTUATOR DESIGN AND INTEGRATION

A pair of TSW actuators [37] was embedded in the fold line of the origami structure. These actuators could actively fold the origami using the twisting motion of the SMA wire (see Fig. 11) bidirectionally, as shown in Supplementary Movie. A simple SMA wire was prestrained by twisting and each end, which was aligned along the middle of the fold line, was fixed to a facet, as shown in Fig. 11(a). When the wire was heated, it twisted and generated a torque, rotating the joint [Fig. 11(b) and (c)]. Because the SMA could be easily actuated (i.e., heated by electricity through the wire), selective and addressable actuation of the distributed SMA actuators could be achieved.

The design parameters of the TSW actuator were the wire diameter ( $r$ ), torsion length ( $L$ ), and prestrain angle ( $\alpha$ ), as shown in Fig. 11(a). The simplified analytical model and the properties of SMA actuators from a previous work [49], [50] were used to determine the design parameters. The wire diameter is directly related to the torque and actuation frequency, and the torsion length determines the size of the folding joint, which is proportional to cube size. The prestrain angle is the maximum strain angle and can be only adjusted by a multitude of  $\pi$  radian due to geometry. Because the maximum shear strain of the SMA is fixed, the product of the wire diameter and maximum strain angle over the torsion length is constant. The design parameters are determined considering the required rotation angle and torque,

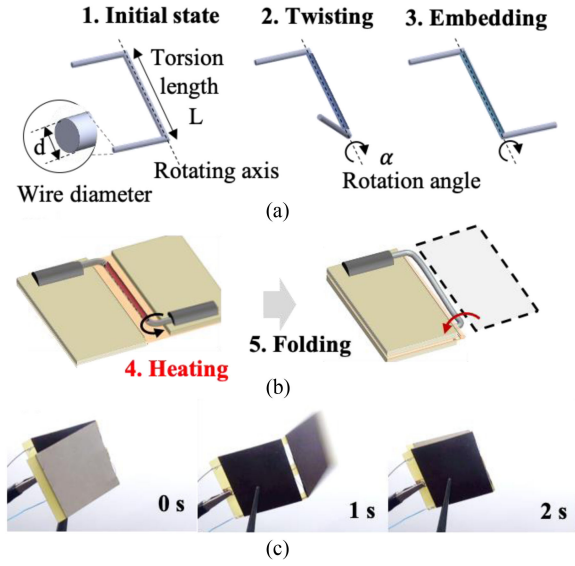


Fig. 11. TSW actuator twists to provide a restoring force, actuating the bidirectional self-folding joint [36]. (a) Design parameters and prestraining process of TSW wire. (b) Active folding joint triggered by heating of TSW actuator. (c) Snapshot of active self-folding joint.

TABLE II  
DESIGN PARAMETERS OF THE TSW ACTUATOR

Properties	Folding	Unfolding
Wire diameter $r$ (mil/ $\mu$ m)	12/300	15/375
Torsion length $L$ (mm)		12
Pre-strain angle $\alpha$ (degree)		360

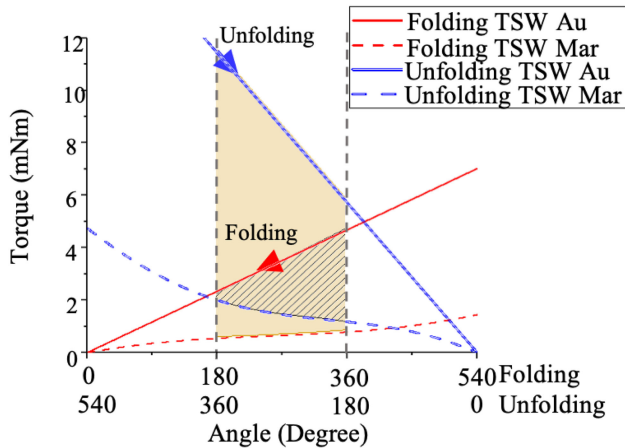


Fig. 12. Torque generated by each TSW actuator in an antagonistic pair. Colored area represents the net energy generated by the actuator pair when the origami block is folding, while the dashed area represents the net energy when unfolding.

and multiple sets of parameters exist. Table II presents the design parameters selected for the origami block. Fig. 12 shows the torque profile of the selected TSW actuator pair. Each actuator is prestrained by  $360^\circ$  and if heated, rotates in the direction of decreasing prestrain angle. The torque of the actuated TSW, which is in the Austenite (Aus) state, should always be larger

than that of the unactuated TSW, which is in the Martensite (Mar) state, until it reaches the target position. Folding and unfolding actuators are set to have different torque because the torque needed for unfolding is larger than the torque needed for folding due to the structure's own weight.

Owing to the highly nonlinear characteristic of the SMA, the actuation performance of the block strongly depends on the location of the actuators, even though they might have identical physical properties. The overconstrained condition allows any flexure to trigger the morphing of the entire structure; however, each flexure requires a different torque profile. These characteristics need to be considered for actuator integration. The performance of the TSW actuator is determined by the diameter of the wire and its length. The maximum force increases with the wire diameter; however, the actuation period also increases owing to the cooling time. Thus, the morphing speed decreases as the required torque increases. Therefore, it is advantageous to select a location that requires the minimal torque to realize a fast repetitive actuation.

The required torque profile for each flexure is derived from the following virtual work principle of a deformable body. The total internal virtual work  $U$  performed by the material stress and strain is equal to the total external virtual work

$$U = \sum_{mn} \int \tau_{mn} d\theta_{mn} + \sum_k \int F_k dr_k \quad (17)$$

where  $\tau_{mn}$  and  $\theta_{mn}$  are the actuator's torque and angle displacement, respectively, when positioned on the flexure connecting the  $m$ th and  $n$ th facet;  $F_k$  and  $r_k$  are the structure's internal force and displacement, respectively, applied in the  $j$ -direction. By assuming that the payload  $P$  in the vertical direction is the only required force for the system, and that the actuator is attached to the flexure connecting the  $m$ th and  $n$ th facet, the required torque can be expressed as follows:

$$\begin{aligned} \delta U &= \tau_{mn} \delta \theta_{mn} - P \delta h \\ \tau_{mn} &= \frac{\delta U}{\delta \theta_{mn}} + P \frac{\delta h}{\delta \theta_{mn}} = U_{,\theta_{mn}} + P h_{,\theta_{mn}}. \end{aligned} \quad (18)$$

The names of the facets and the locations of the flexure pairs are presented in Fig. 6. For example, the F1–F2 flexure indicates the flexure that connects facets F1 and F2. Fig. 13(a) and (b) shows the profile of the internal energy derivative  $U_{,\theta}$  and the block's height derivative  $h_{,\theta}$  for each flexure as a function of the actuation angle, from which the required torque required is determined. The internal energy and height were determined considering the result of the physical property design section when the flexure ratio is 7.5%. We assumed the symmetry of the structure so that flexure which is not plotted is identical with other flexure plotted, e.g., F1–F2 flexure is identical with F1–F5 flexure. In Fig. 13(a) and (b), the flexure that requires the minimum torque is the F2–F3 flexure in the middle of the side face. Therefore, the F2–F3 flexure and F5–F6 flexure which was placed symmetrically were selected as the active joint to be driven by the TSW actuator, as shown in Fig. 13(c).

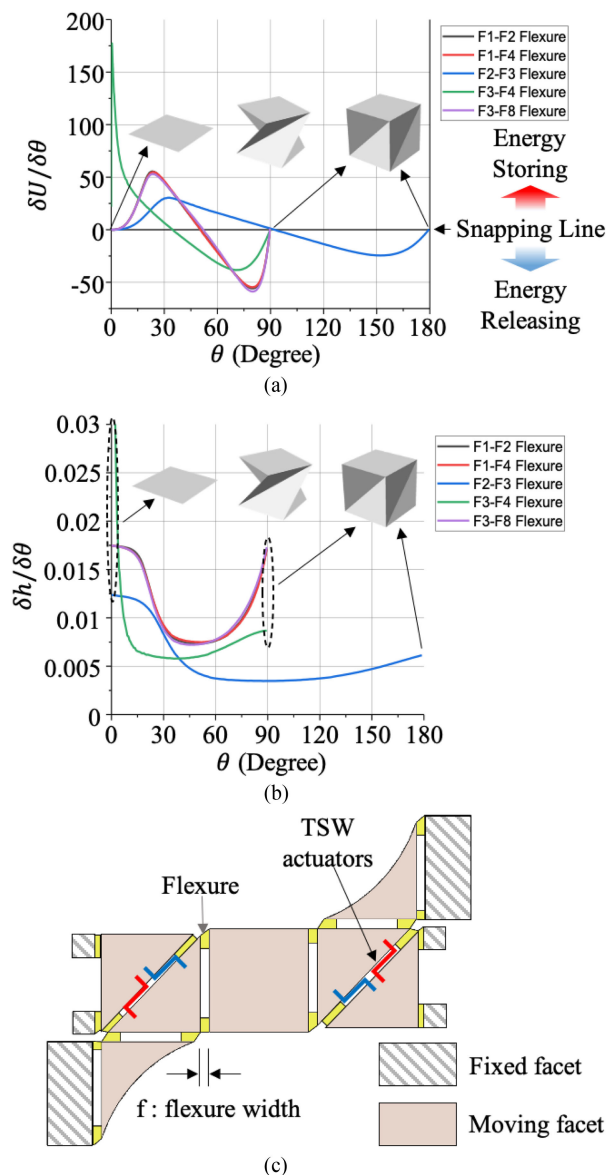


Fig. 13. Stress-strain analysis for actuator integration. (a) Internal energy variation as a function of the folding angle of each flexure. Large changes in the internal energy require a large torque. (b) Height variation as a function of the folding angle of each flexure. Rapid changes in the height require a large torque. (c) Unfolded planar view of the origami block showing the flexures and optimal TSW actuator mapping on the pattern.

## V. DEMONSTRATION

The demonstration was performed using a single block with a side length and mass of 50 mm and 6 g, respectively. Each morphing took only a few seconds, and the fully deployed block could support at least 20 times its own weight in the vertical direction. As illustrated in Fig. 14(a) and Supplementary Movie, the single block could transform between a 2-D flat sheet and a 3-D cubic block with the application of a constant current of 1.2 A to the module.

By stacking up the origami block in the vertical direction, we built a three-story column with individually actuating origami

blocks, as illustrated in Fig. 14(b) and Supplementary Movie. To overcome the stability issue during the morphing, the blocks were developed in order from the bottom layer, and the folding was performed in the reverse order.

Using a multilayer arrangement of these origami blocks, the system could be expanded in a 3-D space. We built a modular reconfigurable structure in a  $3 \times 3$  matrix form with identical three-story columns. As illustrated in Fig. 14(c) and Supplementary Movie, the shape of the three-layer block could be changed through the actuation of the individual blocks by a command in a programmable manner.

## VI. DISCUSSION

In this study, we proposed a design strategy for an actuation mechanism to complement the deficiencies of the TSW actuator and presented an origami-based shape-programmable architecture with an actuation capability that has not been achievable in existing programmable origamis. We presented a shape-shifting architecture as a representative application; however, the scope of application is not necessarily limited to this form. The design method that takes advantage of the structural characteristic can be used in a variety of situations in which smart material-based actuators are required owing to the size and weight limitations. Fig. 15(a) and Supplementary Movie show a deployable gripper as an example. The gripper can be unfolded into a deployed state while maintaining its shape without any additional energy owing to the inherent structural bistability. Another potential property that we wish to highlight is the flexibility of the system with modularization. Fig. 15(b) and Supplementary Movie demonstrate the possibility of modularization of single block. Each block consists of morphing hardware and magnet electrodes which can deliver power and signal input. The blocks can be assembled and disassembled to each other in the vertical direction freely via embedded magnet electrodes in the top and bottom facets. The bottom layer is connected to the power source and transfers all the signal lines for each block. Through modularization, blocks can be easily replaced and rearranged.

The resolution of the system is determined by the essential performance factors and the limitations of the proposed system. If the system is implemented using the stacking method over a 2-D area as in the current form, the resolution is limited by the payload of each block, which limits the number of stackable layers. The torque of the TSW actuator is closely related to the maximum payload; however, increasing the wire diameter limits the strain of the joint and lowers the actuation frequency. Thus, the optimal actuator parameters can be determined by considering the target system scale.

The scale effect on the structural characteristic was also found to be an important design factor. The reduction in the side length will lead to different results owing to non-scalable factors, such as the adhesive force between the facets and flexure, and the nonlinearity of the material properties. These factors should be strongly dependent on the external environment and material composition and need to be determined through on-site tests.

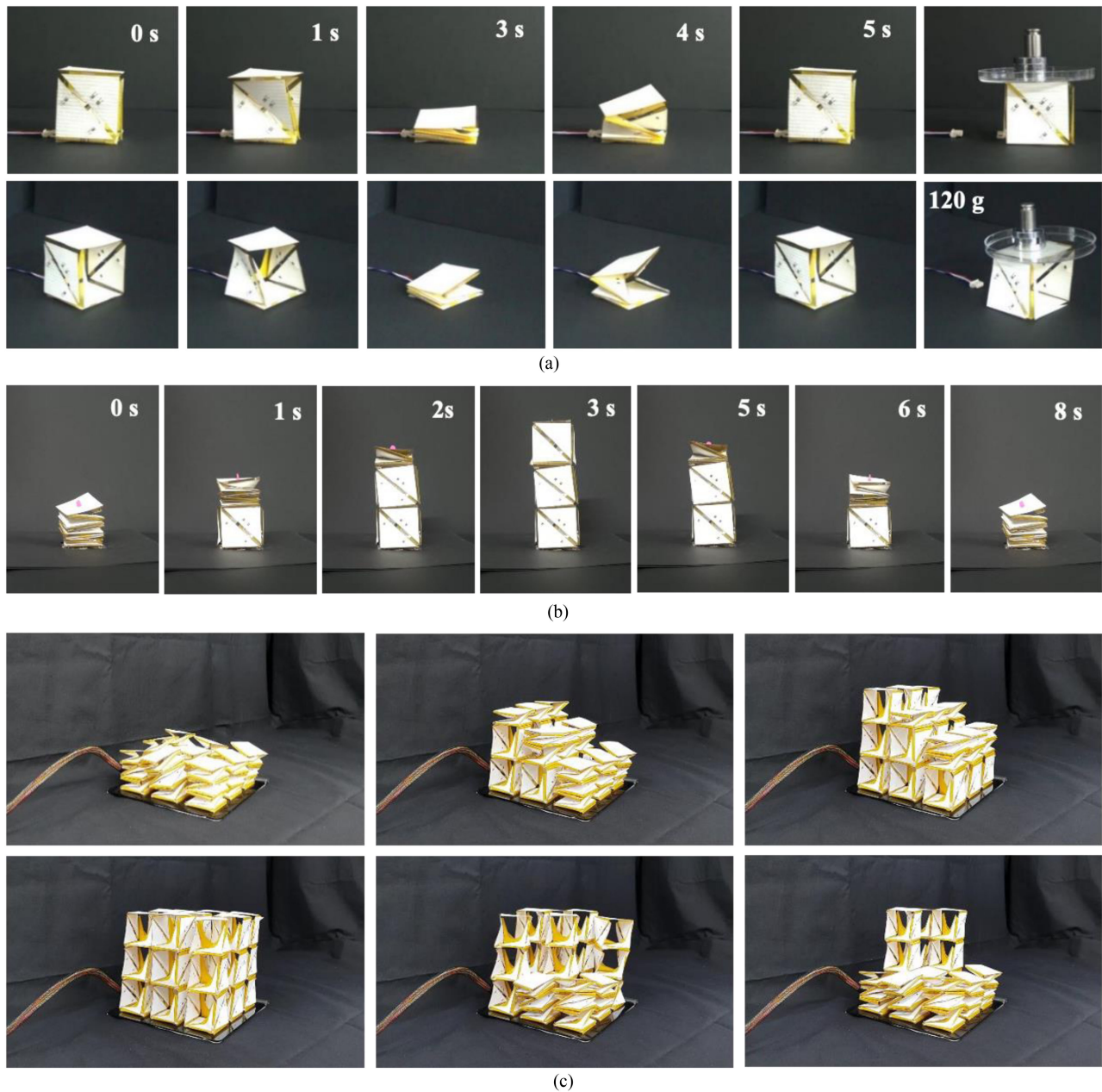


Fig. 14. Implementation of the origami blocks and the shape-programmable architecture. (a) Single morphing origami block can change from a 2-D sheet to 3-D cubic shape within seconds for each transformation, and it exhibits structural stability at each target state. The block can support more than 20 times its own weight without the actuator force. (b) Transformation of multilayered blocks. (c) Shape-changing performance of the  $3 \times 3 \times 3$  multiblock system, which can be reconfigured into diverse 3-D configurations from a flat initial state.

Furthermore, because shape deformations are achieved only by varying the height, the shape transformation flexibility of the current system is limited. However, this aspect could be diversified to multiple directions by utilizing various types of unit blocks, thereby increasing the system transformation dimension. In this case, the achievable force scale remains a major factor in determining the resolution.

The reliability of the system becomes an increasingly critical issue as the number of blocks increases to improve the resolution. Owing to the inconsistencies in the manual fabrication process

and actuator performance, the behavior of each block may not be uniform, resulting in a reliability problem. We anticipate that the use of automated laminating and actuator assembly processes can solve this problem. In addition, even though the system does not require an accurate angle control, large-scale systems require state feedback to achieve energy efficiency and stable performance. The discretized movement of the system lowers the required specification of the state sensing; therefore, the use of simple feedback methods, such as a mechanical contact switch, could provide sufficient state data.

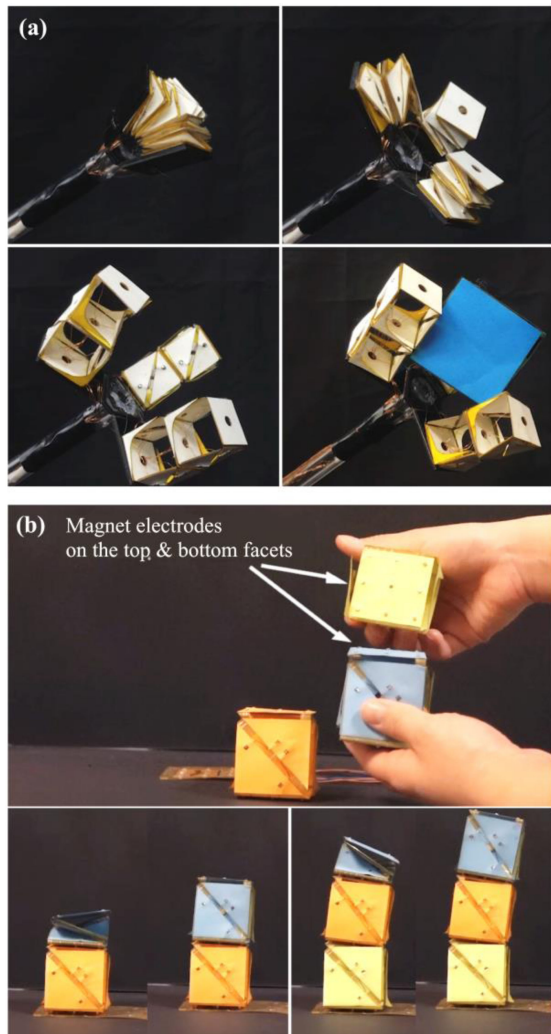


Fig. 15. Applications of morphing origami blocks. (a) Deployable gripper. (b) Modularized origami blocks, which can be disassembled and rearranged in any vertical sequence.

#### ACKNOWLEDGMENT

The authors would like to thank J. J.-R. Song for directing and creating the demonstration video.

#### REFERENCES

- [1] J. H. Brackenbury, "Wing folding and free-flight kinematics in Coleoptera (Insecta): A comparative study," *J. Zoology*, vol. 232, no. 2, pp. 253–253, 1994.
- [2] H. Kobayashi, B. Kresling, and J. F. Vincent, "The geometry of unfolding tree leaves," *Proc. Roy. Soc. B, Biol. Sci.*, vol. 265, no. 1391, pp. 147–154, 1998.
- [3] L. Mahadevan and S. Rica, "Self-organized origami," *Science*, vol. 307, no. 5716, pp. 1740–1740, 2005.
- [4] B. Kresling, "Coupled mechanisms in biological deployable structures," in *Proc. IUTAM-IASS Symp. Deployable Struct., Theory Appl.*, 2000, pp. 229–238.
- [5] K. Miura, "Method of packaging and deployment of large membranes in space," *Inst. Space Astron. Sci.*, no. 618, pp. 1–9, 1985.
- [6] E. Morris, D. A. McAdams, and R. Malak, "The state of the art of origami-inspired products: A review," in *Proc. ASME Int. Des. Eng. Tech. Conf. Comput. Inf. Eng. Conf. Amer. Soc. Mech. Eng. Digital Collection*, 2016.
- [7] P. Birkmeyer, K. Peterson, and R. S. Fearing, "DASH: A dynamic 16g hexapedal robot," in *Proc. IEEE/RJS Int. Conf. Intell. Robot. Syst.*, 2009, pp. 2683–2689.
- [8] R. J. Wood, "The first takeoff of a biologically inspired at-scale robotic insect," *IEEE Trans. Robot.*, vol. 24, no. 2, pp. 341–347, Apr. 2008.
- [9] J. S. Koh *et al.*, "Jumping on water: Surface tension-dominated jumping of water striders and robotic insects," *Science*, vol. 349, no. 6247, pp. 517–521, 2015.
- [10] S. J. Kim, D. Y. Lee, G. P. Jung, and K. J. Cho, "An origami-inspired, self-locking robotic arm that can be folded flat," *Sci. Robot.*, vol. 3, no. 16, 2018, Art. no. eaar2915.
- [11] W. Kim *et al.*, "Bioinspired dual-morphing stretchable origami," *Sci. Robot.*, vol. 4, no. 36, 2019, Art. no. eaay3493.
- [12] S. Miyashita, S. Guitron, S. Li, and D. Rus, "Robotic metamorphosis by origami exoskeletons," *Sci. Robot.*, vol. 2, no. 10, 2017, Art. no. eaao4369.
- [13] Z. Zhakypov, K. Mori, K. Hosoda, and J. Paik, "Designing minimal and scalable insect-inspired multi-locomotion millirobots," *Nature*, vol. 571, no. 7765, pp. 381–386, 2019.
- [14] D. Y. Lee, S. R. Kim, J. S. Kim, J. J. Park, and K. J. Cho, "Origami wheel transformer: A variable-diameter wheel drive robot using an origami structure," *Soft Robot.*, vol. 4, no. 2, pp. 163–180, 2017.
- [15] K. Kuribayashi *et al.*, "Self-deployable origami stent grafts as a biomedical application of Ni-rich TiNi shape memory alloy foil," *Mater. Sci. Eng. A, Struct. Mater. Properties Microstruct. Process.*, vol. 419, pp. 131–137, 2006.
- [16] S. Mintchev, L. Daler, G. L'Eplattenier, L. Saint-Raymond, and D. Floreano, "Foldable and self-deployable pocket sized quadrotor," in *Proc. IEEE Int. Conf. Robot. Autom.*, 2015, pp. 2190–2195.
- [17] C. D. Onal, R. J. Wood, and D. Rus, "Towards printable robotics: Origami-inspired planar fabrication of three-dimensional mechanisms," in *Proc. IEEE Int. Conf. Robot. Autom.*, 2011, pp. 4608–4613.
- [18] S. Felton, M. Tolley, E. Demaine, D. Rus, and R. Wood, "A method for building self-folding machines," *Science*, vol. 345, no. 6197, pp. 644–646, 2014.
- [19] A. M. Hoover and R. S. Fearing, "Fast scale prototyping for folded millirobots," in *Proc. IEEE Int. Conf. Robot. Autom.*, 2008, pp. 886–892.
- [20] J. P. Whitney, P. S. Sreetharan, K. Y. Ma, and R. J. Wood, "Pop-up book MEMS," *J. Micromech. Microeng.*, vol. 21, no. 11, 2011, Art. no. 115021.
- [21] E. Demaine and J. O'Rourke, *Geometric Folding Algorithms: linkages, Origami, Polyhedra*. Cambridge, MA, USA: Cambridge Univ. Press, 2007.
- [22] E. D. Demaine, M. L. Demaine, and J. S. Mitchell, "Folding flat silhouettes and wrapping polyhedral packages: New results in computational origami," *Comput. Geom., Theory Appl.*, vol. 16, no. 1, pp. 3–21, 2000.
- [23] E. Hawkes *et al.*, "Programmable matter by folding," *Proc. Nat. Acad. Sci.*, vol. 107, no. 28, pp. 12441–12445, 2010.
- [24] Q. Ge, C. K. Dunn, H. J. Qi, and M. L. Dunn, "Active origami by 4D printing," *Smart Mater. Struct.*, vol. 23, no. 9, 2014, Art. no. 094007.
- [25] J. T. Overvelde *et al.*, "A three-dimensional actuated origami-inspired transformable metamaterial with multiple degrees of freedom," *Nature Commun.*, vol. 7, 2016, Art. no. 10929.
- [26] M. Schenk and S. D. Guest, "Geometry of Miura-folded metamaterials," *Proc. Nat. Acad. Sci.*, vol. 110, no. 9, pp. 3276–3281, 2013.
- [27] J. L. Silverberg *et al.*, "Using origami design principles to fold reprogrammable mechanical metamaterials," *Science*, vol. 345, no. 6197, pp. 647–650, 2014.
- [28] Z. Zhai, Y. Wang, and H. Jiang, "Origami-inspired, on-demand deployable and collapsible mechanical metamaterials with tunable stiffness," *Proc. Nat. Acad. Sci.*, vol. 115, no. 9, pp. 2032–2037, 2018.
- [29] H. Fang, S. C. A. Chu, Y. Xia, and K. W. Wang, "Programmable self-locking origami mechanical metamaterials," *Adv. Mater.*, vol. 30, 2018, Art. no. 1706311.
- [30] J. T. B. Overvelde, J. C. Weaver, C. Hoberman, and K. Bertoldi, "Rational design of reconfigurable prismatic architected materials," *Nature*, vol. 541, no. 7637, pp. 347–352, 2017.
- [31] L. H. Dudte, E. Vouga, T. Tachi, and L. Mahadevan, "Programming curvature using origami tessellations," *Nature Mater.*, vol. 15, no. 5, pp. 583–588, 2016.
- [32] D. M. Sussman *et al.*, "Algorithmic lattice kirigami: A route to pluripotent materials," *Proc. Nat. Acad. Sci.*, vol. 112, no. 24, pp. 7449–7453, 2015.
- [33] S. Kamrava, D. Mousanezhad, S. M. Felton, and A. Vaziri, "Programmable origami strings," *Adv. Mater. Technol.*, vol. 3, no. 3, 2018, Art. no. 1700276.
- [34] C. H. Belke and J. Paik, "Mori: A modular origami robot," *IEEE/ASME Trans. Mechatronics*, vol. 22, no. 5, pp. 2153–2164, Oct. 2017.
- [35] Y. Kim, H. Yuk, R. Zhao, S. A. Chester, and X. Zhao, "Printing ferromagnetic domains for untethered fast-transforming soft materials," *Nature*, vol. 558, no. 7709, pp. 274–279, 2018.

- [36] Z. Zhakypov, M. Mete, J. Fiorentino, and J. Paik, "Programmable fluidic networks design for robotic origami sequential self-folding," in *Proc. IEEE Int. Conf. Soft Robot.*, 2019, pp. 814–820.
- [37] J. S. Koh, S. R. Kim, and K. J. Cho, "Self-folding origami using torsion shape memory alloy wire actuators," in *Proc. ASME Int. Des. Eng. Tech. Conf. Comput. Inf. Eng. Conf.*, 2014.
- [38] S. R. Kim, D. Y. Lee, J. S. Koh, and K. J. Cho, "Fast, compact, and lightweight shape-shifting system composed of distributed self-folding origami modules," in *Proc. IEEE Int. Conf. Robot. Autom.*, 2016, pp. 4969–4974.
- [39] S. D. Guest and S. Pellegrino, "The folding of triangulated cylinders, part I: Geometric considerations," *J. Appl. Mech.*, vol. 61, pp. 773–777, 1994.
- [40] S. Ishida, H. Uchida, and I. Hagiwara, "Vibration isolators using nonlinear spring characteristics of origami-based foldable structures," *Trans. Jpn Soc. Mech. Eng.*, vol. 80, p. 820, 2014.
- [41] H. Yasuda, T. Tachi, M. Lee, and J. Yang, "Origami-based tunable truss structures for non-volatile mechanical memory operation," *Nature Commun.*, vol. 8, no. 1, 2017, Art. no. 962.
- [42] J. Cai, Y. Liu, R. Ma, J. Feng, and Y. Zhou, "Nonrigidly foldability analysis of Kresling cylindrical origami," *J. Mechanisms Robot.*, vol. 9, no. 4, 2017, Art. no. 041018.
- [43] J. Cai, X. Deng, Y. Zhang, J. Feng, and Y. Zhou, "Folding behavior of a foldable prismatic mast with Kresling origami pattern," *J. Mechanisms Robot.*, vol. 8, no. 3, 2016, Art. no. 031004.
- [44] J. Cai, X. Deng, Y. Zhou, J. Feng, and Y. Tu, "Bistable behavior of the cylindrical origami structure with Kresling pattern," *J. Mech. Des.*, vol. 137, no. 6, 2015, Art. no. 061406.
- [45] Y. Chen, R. Peng, and Z. You, "Origami of thick panels," *Science*, vol. 349, no. 6246, pp. 396–400, 2015.
- [46] T. Tachi, "Simulation of rigid origami in Origami 4," in *Proc. 4th Int. Conf. Origami Sci. Math. Educ.*, 2009, no. 8, pp. 175–187.
- [47] J. A. Faber, A. F. Arrieta, and A. R. Studart, "Bioinspired spring origami," *Science*, vol. 359, no. 6382, pp. 1386–1399, 2018.
- [48] *Dupont Kapton Polyimide Film General Specifications, Bulletin GS-96-7*. [Online]. Available: <http://www.dupont.com/kapton/general/H-38479-4.pdf>
- [49] S. M. An, J. Ryu, M. Cho, and K. J. Cho, "Engineering design framework for a shape memory alloy coil spring actuator using a static two-state model," *Smart Mater. Struct.*, vol. 21, no. 5, 2012, Art. no. 055009.
- [50] J. S. Koh, "Design of shape memory alloy coil spring actuator for improving performance in cyclic actuation," *Materials*, vol. 11, no. 11, 2018, Art. no. 2324.



**Sa-Reum Kim** (Student Member, IEEE) received the B.S. and M.S. degrees in mechanical engineering from Seoul National University, Seoul, South Korea, in 2015 and 2017, respectively. She is currently working toward the Ph.D. degree in mechanical engineering with Biomimetic Millisystems Laboratory, University of California at Berkeley, Berkeley, CA, USA.

Her research interests include small-scale robot and mechanism design with smart structures and actuators.



**Dae-Young Lee** received the B.S. degree from Pohang University of Science and Technology, Pohang, South Korea, in 2011, and the M.S. and Ph.D. degrees from Seoul National University, Seoul, South Korea, in 2013 and 2017, respectively, all in mechanical engineering.

He is currently a Postdoctoral Fellow with Harvard Microrobotics Laboratory, Cambridge, MA, USA. His research interests include soft robotics, origami-inspired design, and novel-mechanisms using smart materials, structures, and actuators.



**Sang-Joon Ahn** (Student Member, IEEE) received the B.S. degree in mechanical engineering from Yonsei University, Seoul, South Korea, in 2018. He is currently working toward the Ph.D. degree in mechanical engineering with the Biorobotics Laboratory, Seoul National University, Seoul, South Korea.

His research interests include soft robotics and 3-D/4-D printing of smart materials and structures.



**Je-Sung Koh** (Member, IEEE) received the B.S. and Ph.D. degrees in mechanical and aerospace engineering from Seoul National University, Seoul, South Korea, in 2008 and 2014, respectively.

He was a Postdoctoral Fellow with Harvard Microrobotics Laboratory, Cambridge, MA, USA, until 2017. He is currently an Assistant Professor of Mechanical Engineering with Ajou University, Suwon, South Korea. His research interests include biologically inspired, small-scale robot design, and soft robots.



**Kyu-Jin Cho** (Member, IEEE) received the B.S. and M.S. degrees from Seoul National University, Seoul, South Korea, in 1998 and 2000, respectively, and the Ph.D. degree in mechanical engineering from the Massachusetts Institute of Technology, Cambridge, MA, USA, in 2007.

He was a Postdoctoral Fellow with Harvard Microrobotics Laboratory, Cambridge, MA, USA, until 2008. At present, he is a Professor of Mechanical and Aerospace Engineering and the Director of the BioRobotics Laboratory and Soft Robotics Research Center with Seoul National University. His research interests include biologically inspired robotics, soft robotics, soft wearable devices, novel mechanisms using smart structures, and rehabilitation and assistive robotics.

Prof. Cho was the recipient of the 2014 IEEE RAS Early Academic Career Award, 2014 ASME Compliant Mechanism Award, 2013 IROS Best Video Award, and 2013 KSPE Paik Am Award.